Chemistry Europe
European Chemical Societies Publishing
Batteries & Supercaps

RESEARCH ARTICLE OPEN ACCESS

Accelerated Reaction Kinetics in Quasi-Solid-State Li–S Batteries via $Li_{10}GeP_2S_{12}$: From Mechanistic Insights to Pouch Cell Realisation

Huanxin Li[1,2,3] | Boyi Pang[1,2,3] | Liam Bird[3,4] | Yuhan Liu[2,3] | Francesco Iacoviello[2] | Sharad Amin[5] | Gareth Hartley[5] | Adrien Amigues[5] | Paul R. Shearing[3,4] | Rhodri Jervis[1,2,3] | James B. Robinson[1,2,3]

[1]Advanced Propulsion Lab (APL), University College London, Marshgate, London, UK | [2]Electrochemial Innovation Lab (EIL), University College London, London, UK | [3]Faraday Institution, Quad One, Becquerel Avenue, Harwell Science and Innovation Campus, Didcot, UK | [4]Zero Institute, Holywell House, Osney Mead, University of Oxford, Oxford, UK | [5]Gelion Ltd, London, UK

Correspondence: Huanxin Li (huanxin.li@ucl.ac.uk) | James B. Robinson (j.b.robinson@ucl.ac.uk)

Received: 9 February 2026 | **Revised:** 13 May 2026 | **Accepted:** 19 May 2026

Keywords: chemical engineering | chemical kinetics | electrochemistry | electrode | electrolyte | kinetics | materials science | microscale chemistry | polysulfide | sulfur

ABSTRACT

Lithium–sulfur (Li–S) batteries are emerging as promising next-generation chemistry due to their ultra-high energy density, potential for improved safety and the promise of secure global supply chains. Unlike conventional Li–S systems, so-called quasi-solid-state (QSS) Li–S batteries employ electrolytes that sparingly solvate polysulfide species suppressing the 'shuttle effect' and enhancing cycling stability. However, to date the practical deployment of QSS cells has been hindered by comparatively sluggish kinetics and limited stability; furthermore, insights into the mechanism of operation of this cell type remain scarce. Here, we demonstrate improved kinetics, through the incorporation of $Li_{10}GeP_2S_{12}$. We explore this performance enhancement by examining degradation pathways using in situ X-ray computed tomography imaging and complimentary electrochemical techniques. We also propose a concise methodology to quantify the sulfur intermediate according to cyclic voltammetry profiles, revealing the presence of sparingly soluble Li_2S_x ($x = 4.96$) and QSS Li_2S_y ($y = 2.53$) during cycling in our system. Tomographic imaging clearly identifies morphological evolution during cycling suggesting microscale changes to the electrode as a key cause of capacity decay. Protocols for electrode fabrication, electrolyte preparation, and cell assembly were established, achieving a sulfur loading $> 4\ mg_S\ cm^{-2}$, a capacity $> 1200\ mAh\ g_S^{-1}$, and stability with 2.8% capacity loss over 100 cycles.

1 | Introduction

Lithium–sulfur (Li–S) batteries have emerged as a transformative energy storage technology due to sulfur's very high capacity of $1675\ mAh\ g^{-1}_S$ which, when coupled with a Li electrode, offers the potential for practical energy densities that greatly supersede those achievable using conventional lithium-ion batteries [1–6]. This advantage is primarily attributed to the multielectron redox reactions of sulfur. Additionally, the low cost, natural abundance, and environmental benignity of sulfur make Li–S an attractive candidate for a next-generation battery technology [7]. Given the potential for exceptionally high gravimetric energy density of Li–S cells, alongside their comparatively low-rate performance, initial beachhead applications for this chemistry are expected to be in manned and unmanned aerospace sectors, where weight is critically constrained [8, 9].

Practical deployment of conventional Li–S cells has been hindered by several intrinsic performance challenges. The dissolution of intermediate lithium polysulfides (Li_2S_x, $2 \le x \le 8$) into the liquid electrolyte is widely known to result in the "shuttle effect," causing active material loss and rapid capacity degradation [10–12]. It has

been noted that the poor kinetics of Li_2S_6 conversion to lower-chained polysulfides and rapid cross over of this species to the anode are likely to result in capacity fade during cell operation [13]. Furthermore, the need to dissolve sulfur into the electrolyte has necessitated electrolyte volumes which are far larger than those observed in Li-ion cells, often making up >40% of the mass of the cell, which significantly impacts the realisable gravimetric energy density of the cell [14]. In addition to this large electrolyte volume, the insulating nature of sulfur and its end discharge product, lithium sulfide (Li_2S), requires the use of conductive additives, further reducing the overall energy density [15]. To maximise the potential of this chemistry, there is a need to stabilise the sulfur species, ensure lean electrolyte operation and maximise the active components in the positive electrode. Achieving this will enable the deployment of a cell which exceeds those practically realisable using conventional Li–S chemistry [16].

Previous advancements in battery materials science have introduced a variety of solutions for mitigating the 'shuttle effect' and stabilising polysulfide intermediates [15]. Composite positive electrodes, for example, have emerged as a key focus area. By incorporating conductive carbon frameworks, these positive electrodes enhance electron transport and provide sites for the adsorption of polysulfides, minimising their dissolution into the electrolyte [17, 18]. Further innovations, such as the inclusion of metal sulfides, oxides, or carbides as catalytic agents, have demonstrated the ability to accelerate the redox reactions of sulfur species, thereby improving the overall efficiency of the battery [2, 16, 19]. While positive electrodes employing high loadings of elemental sulfur have shown exceptional energy densities, they often suffer from low cycle life. In contrast, lithium–sulfur batteries using sulfurised polyacrylonitrile (Li-SPAN) positive electrodes offer significantly improved cycling stability and longevity. This enhanced durability is largely attributed to the chemical bonding of sulfur within the polymer matrix, which suppresses the polysulfide shuttle effect and maintains structural integrity during repeated charge–discharge cycles. However, despite these benefits, SPAN-based positive electrodes impose a practical limit on the maximum sulfur loading (≈40 wt%), thereby capping the energy density achievable with this cell format and reducing their competitiveness in applications where ultra-high energy density is essential [20–23].

While conventional Li–S batteries utilise liquid electrolytes that provide high ionic conductivity, they fail to effectively suppress polysulfide migration. In contrast, all-solid-state electrolytes offer excellent mechanical stability and mitigate the shuttle effect but often suffer from limited ionic conductivity and compatibility concerns with sulfur positive electrodes due to the large expansion which occurs upon conversion of sulfur to Li_2S [24, 25]. To address these challenges [26], various materials have been explored, including polymer-based electrolytes [24], ionic liquids [27, 28], and sulfide-based solid electrolytes [29].

Quasi-solid-state (QSS) Li–S batteries present a promising strategy to tackle these challenges. By combining the benefits of liquid electrolytes with high salt concentrations, pseudo-solid-state conversion mechanisms of sulfur species can be induced. QSS systems limit polysulfide dissolution while maintaining sufficient ionic conductivity. This approach offers the highly attractive opportunity to reduce the electrolyte loading in cells (commonly referred to as the electrolyte to sulfur or E/S ratio) significantly, which, if realised would enable ultra-high gravimetric energy densities, or the freedom to reduce the sulfur loading in the positive electrode by extension improving the electrical conductivity or incorporating alternative components. However, highly saturated electrolytes tend to have high gravimetric density due to high salt content and the use of high concentrations of halogenated viscosity modifiers. Whilst QSS technology is still in its infancy, recent studies have shown that the design of composite positive electrodes, and the optimisation of electrolyte formulations can yield robust interfaces and enhance battery performance [30–32]. As discussed previously, reports have suggested that the Li_2S_6 polysulfide is the dominant factor in the polysulfide shuttle in a conventional Li–S cell, therefore a hypothetical design for a QSS cell should focus on constraining the formation of this or accelerating its further conversion to Li_2S_4 and avoiding its formation via any disproportionation reaction which can occur within the cell [13]. To achieve this, the electrolyte is a critical component in QSS Li–S batteries. The hybrid approach in QSS Li–S batteries employs localised high-concentration liquid electrolytes to facilitate the solid-state conversion of sulfur species, striking a balance between ionic mobility and structural stability. Several such electrolytes have been investigated [33, 34], although the kinetics reported remain suboptimal and the fundamental operating mechanisms are still ambiguous. Solid-state electrolytes such as lithium thiophosphate (LGPS) have garnered significant attention for their high ionic conductivity and compatibility with sulfur-based positive electrodes [35]. A semisolid positive electrode concept combining carbon, sulfur, and solid electrolyte was introduced to ensure both electronic and ionic conductivity, while a dimethoxyethane (DME)/LiFSI/hydrofluoroether-based electrolyte demonstrated stability and compatibility in both coin and pouch cells [34, 35]. However, the integration of LGPS into the positive electrode for Li–S batteries, which could significantly enhance reaction kinetics and capacity retention—thereby establishing QSS batteries as a viable pathway for next-generation energy storage—has been largely unexplored [35].

Besides, the success of QSS Li–S batteries hinges on a thorough understanding of the sulfur redox reactions and the role of intermediates like Li_2S_X, from a mechanistic perspective. These intermediates are central to the electrochemical processes occurring within the battery, dictating its capacity, efficiency, and stability [36, 37]. Advanced characterisation techniques such as in situ X-ray computed tomography (X-CT) and cyclic voltammetry (CV) have provided valuable insights into these mechanisms, visualising the distribution of sulfur species and monitoring the formation and dissolution of polysulfides to track structural changes in real time [38].

Using a reliable, commercially available, sulfur/carbon composite active material (S/C) provided by Gelion as a baseline for the positive electrode, we performed a systematic investigation of conversion mechanisms of sulfur species in QSS electrolytes. The analysis in this study reveals that sulfidic species redistribute in positive electrodes during cycling, even when QSS mechanisms are observed electrochemically. It is believed that sulfur redistribution contributes to capacity fading and spatial restrictions on viable conversion kinetics. By integrating experimental data with theoretical insights, this study elucidates the critical factors influencing battery performance and proposes strategies

to overcome existing challenges. For example, by incorporating 10 wt% of LGPS into the positive electrode, the conversion reactions can be driven even more to a 'solid-to-solid' type mechanism and the kinetics of conversion processes for sulfur species can be increased. The findings presented herein not only advance the fundamental understanding of QSS Li–S batteries but also pave the way for their practical implementation in next-generation energy storage applications.

2 | Materials and Methods

2.1 | Fabrication of Positive Electrodes

The fabrication of positive electrodes and coin cells followed a standardized protocol in which polyvinylidene fluoride-co-hexafluoropropylene (PVDF-HFP, Sigma–Aldrich, 99%) was dissolved in ethyl acetate (EA) at 60°C, followed by the gradual addition of hexane-based solvent (HB) at the same temperature in a 1:1 volume ratio (EA:HB). Subsequently, conductive carbon and PVDF-HFP were dispersed in EA at a mass ratio of 8:1:1 under continuous stirring for 2 h using a magnetic stirrer (Camlab) at 60°C. After the active material was incorporated and thoroughly mixed, the resulting slurry was coated onto aluminium foil (MSE Supplies) at a wet gap thickness of 30 μm and dried at 60°C for ≈30 min. Once dried, the electrodes were cut into circular discs (14 mm in diameter) and assembled into coin cells within an inert glovebox environment, using standard coin cell casings (MTI, Al-Clad CR2032). All fabrication steps were conducted in a dry room. For all cells, Celgard 2000 separators, lithium chips (MTI; thickness: 0.6 mm, diameter: 16 mm, purity: 99%), a single wave spring (MTI, Al-Clad stainless steel for CR2032/CR2016 casings), two stainless steel spacers (MTI; 15.8 × 1.0 mm), and 60 μL of electrolyte were employed.

2.2 | Fabrication of S/C/LGPS Positive Electrodes and Coin Cells

For the S/C/LGPS positive electrode, an additional 10 wt% of LGPS (MSE Supplies, 99%) instead of S/C was thoroughly mixed with positive electrode composite powder at the initial stage to enhance electron transport and improve polysulfide retention. LGPS was incorporated into select samples as a performance-enhancing additive with a similar procedure to that described above used. A new localized high-concentration liquid electrolyte formulation was developed, precisely controlling the ratios of diethylene glycol dimethyl ether (G2), 1,1,2,2-tetrafluoroethyl 2,2,3,3-tetrafluoropropyl ether (TTE), and LiTFSI. The optimised composition (G2:TTE = 1:1 by volume and G2:LiTFSI = 1.5:1 by molar ratio) successfully facilitated the QSS conversion of sulfur species in QSS Li–S batteries.

2.3 | Fabrication of Pouch Cells

Pouch cells were constructed using semiautomated facilities in a dry room (Figure S1) using two single-sided positive electrodes and one double-sided negative electrode in a sandwich-like configuration, which is more commercial relevance to multilayer pouch cells. The negative electrode consisted of a copper foil current collector with lithium foil inlaid on both sides. The electrodes measured 55 × 42 mm. To accommodate the welding lugs, sections of the positive electrodes were partially scraped off using a razor blade. Pouch cell assembly was conducted manually in a controlled dry room environment, where the dew point was maintained below −40°C. Each layer was precisely aligned to ensure uniform contact and minimize the risk of short circuits. Lugs were welded using an ultrasonic metal welder (MTI MSK-4200W, PI-KEM, UK), with aluminium used for the positive electrode (welding time: 0.08 s) and nickel for the negative electrode (welding time: 0.06 s). The electrodes were then sealed within aluminium-plastic films, leaving sufficient space to accommodate gas evolution during cell formation. Electrolyte (1.5 g) was injected using a vacuum injector (MTI MSK-113-CP, PI-KEM, UK). Following sealing, the cells underwent initial activation in a glovebox to stabilize interfacial properties and establish ionic conductivity. After this activation was conducted, excess cell housing material which accommodated gas was removed using a vacuum sealer (MTI MSK-115A-LS, PI-KEM, UK).

2.4 | X-CT Analytical Techniques

Advanced characterisation methods were employed to analyse the structural and compositional evolution of the electrodes. X-CT enabled 3D imaging of the electrode morphology, revealing the spatial distribution of sulfur and lithium sulfide particles. In situ X-CT experiments were conducted at the EIL using micro CT system (X-radia Versa 520) to capture real-time changes during cycling. Micro-CT projections were reconstructed using a filtered back-projection algorithm (XMReconstructor, Carl Zeiss Inc.). The resulting datasets were imported into Avizo 2023.2 (Thermo Fisher Scientific) for segmentation and visualization. A nonlocal means filter was applied to enhance the signal-to-noise ratio.

2.5 | Physicochemical Properties

To assess the stability of LGPS in various common solvents, 1 g of the material was immersed in different solutions for 24 h, followed by complete solvent evaporation. The stability of LGPS in G2-TTE electrolyte was verified by X-ray diffraction (XRD). The samples were then sealed with Kapton tape inside a glovebox to prevent exposure to air. XRD (Stoe STADI-P) was performed on the powder samples (sealed with Kapton tape) using Mo Kα radiation (λ = 0.0709 nm), with data collected over a 2θ range of 2°–40°.

2.6 | Electrochemical Testing

Electrochemical characterisations were performed on both coin and pouch cells to assess their performance under various conditions. CV was conducted at a scan rate of 0.1 mV s^{-1}. Charge–discharge profiles were acquired at C/10 (1C = 1675 mA g^{-1}) within a voltage window of 1.0–4.0 V to analyse the redox behavior of sulfur species. To further investigate the electrochemical mechanisms, electrochemical impedance spectroscopy (EIS) experiments were conducted to determine lithium-ion diffusion coefficients within the cathode material and the kinetics of sulfide conversion reactions. All the electrochemical characterisation was performed using a BioLogic battery test system (BCS-805,

BioLogic). Cell cycling was conducted within a voltage range of 1.0–4.0 V, with an initial cycle at C/20 before transitioning to standard cycling at C/10. Potentiostatic EIS measurements were performed using a Gamry potentiostat (Interface 1010E), with a frequency range of 0.1–1.0 × 10^6 Hz and a voltage perturbation of 5 mV. For EIS of the LGPS, 0.5 g of dried solid was pressed into a small cell (0.8 mm diameter) to form a 5 mm pellet, with lithium chips placed at both ends. EIS measurements were conducted using a Gamry potentiostat (Interface 1010E). The surface morphology of the positive electrode was examined using a digital microscope (Keyence VHX-X1).

3 | Results and Discussion

3.1 | Electrochemical Performance of Coin Cells

Figure 1a presents optical images of the S/C positive electrode with LGPS added along with its binder and carbon additives. Following standard mixing, coating, and drying procedures, this positive electrode achieves a high sulfur loading exceeding 4 mg_S cm^{-2}, a crucial parameter for high-energy-density Li–S batteries (Figure 1b) [14]. The representative X-CT image of this positive electrode (Figure 1c) reveals a composite morphology comprising flakes and particles, with the latter identified as sulfur species. This morphology aligns with the structures within the same series of S/C electrodes (Figures S10–S13), exhibiting comparable diameter, sphericity, and a median particle size of ≈5 μm (Table S1).

The CV profiles of the standard S/C positive electrodes exhibited well-defined reduction and oxidation peaks, indicative of efficient sulfur conversion and reversible redox reactions. The incorporation of LGPS significantly enhanced the reaction kinetics, as evidenced by the reduced potential gap and increased peak current densities. The Coulombic efficiency of cells containing LGPS remained consistently above 99%, demonstrating rational degrees of sulfur/lithium sulfide conversion during cycling. As shown in

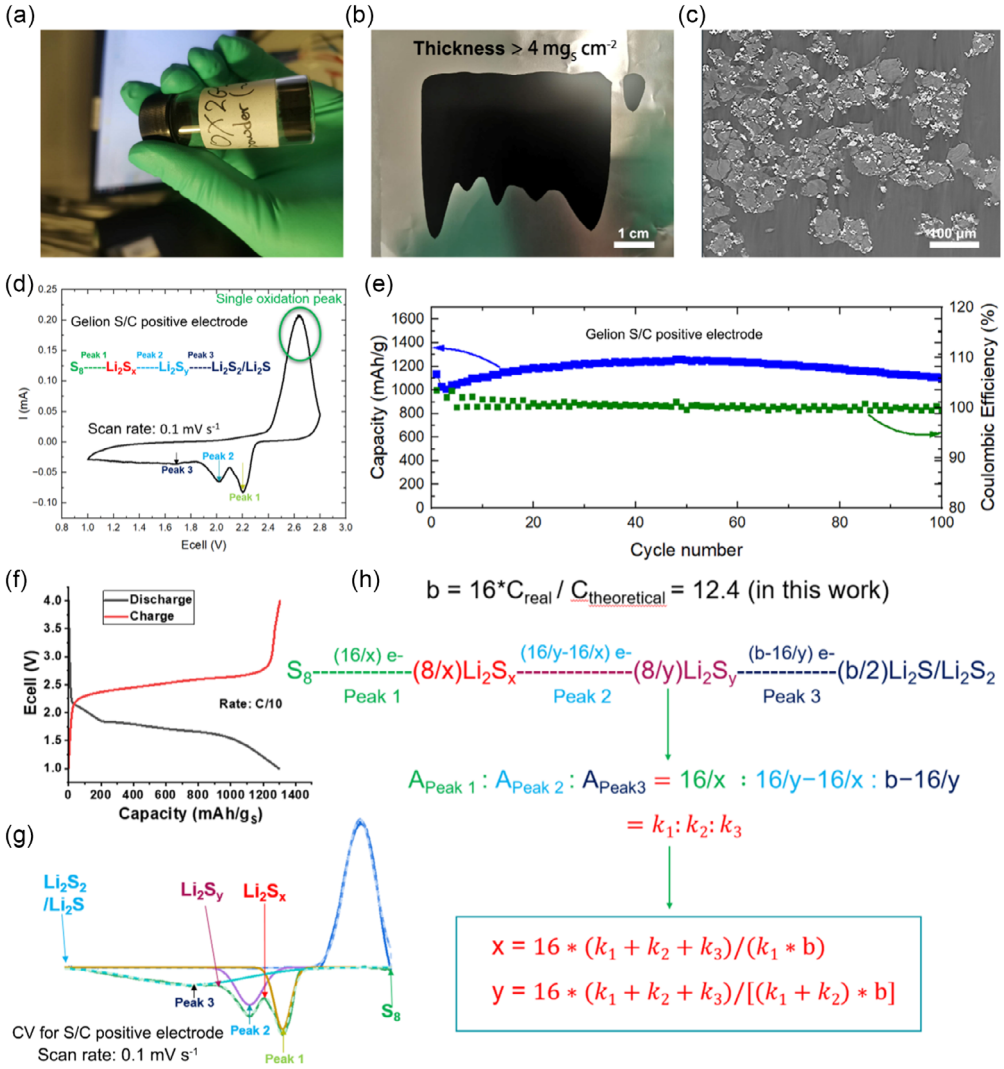

FIGURE 1 | (a) The optical image of a S/C positive electrode; (b) the well-coated S/C positive electrode with a thickness of >4mg_S cm^{-2}; (c) a typical X-CT image of a standard S/C positive electrode; (d) the CV profile of QSS Li–S battery with a standard S/C positive electrode; (e) the cycling profiles for a standard S/C positive electrode in a QSS Li–S battery at a scan rate of 0.1 mV/s; (f) The charge–discharge profiles for S/C positive electrode at C/10; (g) the Gaussian fitting of a CV curve for reduction and oxidation peaks; and (h) calculation of x and y value for the Li_2S_x and Li_2S_y intermediates during reduction.

Figure 1d, the CV curve of the S/C standard positive electrodes deviates significantly from that of conventional Li–S batteries with liquid electrolytes. During the discharge process, two closely spaced reduction peaks appear, in contrast to the well-separated reduction peaks observed in liquid-electrolyte Li–S batteries [19, 39], which typically exhibit a voltage gap of ~200 mV. Additionally, only a single oxidation peak is present during charging, differing from the two oxidation peaks characteristic of conventional Li–S systems. These observations suggest that sulfur conversion occurs via a different mechanism to conventional batteries, which may be described as a QSS process, given the single oxidation step. Moreover, these cells achieve exceptional long-term cycling stability for Li–S batteries. Specifically, the initial discharge capacity of 1134.6 mAh g^{-1} remains at 1102.6 mAh g^{-1} after 100 cycles (Figure 1e), retaining over 97% of its initial capacity. This remarkable stability further indicates that the QSS sulfur conversion mechanism is effective at suppressing long-chained polysulfide formation likely avoiding the production of Li_2S_6, and by extension minimising polysulfide shuttle.

To elucidate the mechanism of sulfur reduction in QSS Li–S batteries, it is crucial to figure out the intermediate lithium polysulfide species (Li_2S_x and Li_2S_y) formed during the reduction process. The initial and final sulfur species are well established as S_8 and Li_2S_2/Li_2S, respectively, and the ratio of Li_2S_2 to Li_2S can be estimated from the ratio of the observed (practical) capacity to the theoretical capacity (1675 mAh/g_S). The S/C positive electrode exhibits a practical capacity of ≈1300 mAh/g_S at C/10 (Figure 1f), indicating incomplete conversion to the final product, Li_2S. We define the parameter b as the actual number of electrons transferred per S_8 molecule relative to the theoretical maximum of 16 for complete conversion to Li_2S. By comparing the practical and theoretical capacities, the b value is determined to be 12.4.

The formation of Li_2S_x and Li_2S_y is closely associated with the number of electrons transferred during the first and second reduction steps. To probe this relationship, the reduction peaks in the CV curves (Figure 1g) were fitted using Gaussian deconvolution after baseline correction, where the baseline was attributed to non-Faradaic capacitance. The CV measurements were performed at the same scan rate as the preceding charge–discharge experiments (Figure 1f) to ensure consistency in the final product composition. The reduction peaks were designated as Peak 1, Peak 2, and Peak 3, and the integrated areas of these peaks collectively match the corresponding oxidation peak area, indicating excellent electrochemical reversibility of the reduction–oxidation processes.

Since the CV measurements were performed at a constant scan rate (0.1 mV s^{-1}), the number of electrons transferred in each step is directly proportional to the integrated areas of Peak 1, Peak 2, and Peak 3, highlighted in yellow, purple, and blue in Figure 1g. The associated chemical processes are summarized in Figure 1h, where the electron transfer numbers following Peaks 1 and 2 are expressed as functions of x and y. The final products, Li_2S_2/Li_2S, after Peak 3 can be determined using the previously defined b value. Based on stoichiometric considerations, the electron transfer numbers are given by 16/x for Peak 1, 16/y−16/x for Peak 2, and b−16/y for the final reduction step. By relating these values to the integrated areas of Peaks 1–3, x and y can be expressed in terms of their ratios, denoted as k_1, k_2, and k_3, yielding the following relationship

$$x = 16(k_1 + k_2 + k_3)/(k_1 \times b)$$

$$y = 16(k_1 + k_2 + k_3)/[(k_1 + k_2) \times \mathrm{b}]$$

where x and y represent the stoichiometric sulfur number in Li_2S_x and Li_2S_y, and k_1, k_2, k_3 correspond to the integrated areas of Peak 1, Peak 2, and Peak 3.

Thus, the integrated area ratios of Peaks 1, 2, and 3 in the CV profile can be used to determine the values of x and y. Generally, when x or $y > 2$, the intermediate polysulfide species (e.g., Li_2S_3, Li_2S_4, Li_2S_5, Li_2S_6, and Li_2S_8) exhibit partial solubility in the electrolyte, whereas when x or $y \leq 2$ (e.g., Li_2S and Li_2S_2), the species remain insoluble, resulting in a solid–solid conversion pathway [40]. In conventional Li–S battery systems, the primary long-chain intermediates (e.g., Li_2S_6) are highly soluble in 1,3-dioxolane/DME electrolytes, promoting polysulfide shuttle and associated capacity loss [19]. However, in this study, using the G2-TTE electrolyte, the integrated areas of Peaks 1, 2, and 3 in the CV curve (Table S2) for sulfur reduction are ≈0.00822, 0.00786, and 0.01553 mW, respectively, yielding an x value of 4.96. This suggests that the mixture of Li_2S_4 and Li_2S_6 (Li_2S_4 dominated) might be the main intermediate species between Peaks 1 and 2. Notably, Li_2S_4 exhibits sparing solubility in G2-TTE electrolyte and will be rapidly converted into short-chain polysulfides in subsequent steps [40]. The y value for the following intermediate stage is 2.53—only slightly above the ideal value of 2—indicating a QSS sulfur conversion mechanism after Peak 2. Although some soluble intermediates (Li_2S_4/Li_2S_6 mixture with Li_2S_4 dominating) are generated in the G2-TTE system, they are swiftly converted into Li_2S_2/Li_2S in the subsequent stage, as evidenced by the fitted CV curves. This CV-based approach provides a quantitative measure of x and y for Li_2S_x and $Li_2S\gamma$ intermediates and is broadly applicable to Li–S battery systems. Importantly, the CV scan rate should match the charge–discharge C-rate to ensure accurate determination of the b value for this quantitative analysis.

3.2 | Structural Evolution Observed via In Situ X-CT

In situ X-CT experiments revealed dynamic morphological changes in the electrode during charge and discharge as mechanistic context. The redistribution of sulfur species and the growth of lithium sulfide (Li_2S) particles were closely monitored, providing critical insights into the interaction between active materials and the electrolyte. These findings highlight the importance of optimising electrode architectures to mitigate structural degradation during cycling. A 0.8 mm Swagelok cell was employed to achieve sufficient X-CT resolution (Figure S4a) [39]. The initial OCP of the cell remained stable at ≈2.85 V (Figure S3), confirming its electrochemical integrity. While absolute dimensions differ from the standard coin cells, the observed sulfur redistribution and crack evolution reflect intrinsic chemo-mechanical responses of the electrode. X-CT imaging provided detailed visualisation of the electrode's structural evolution, enabling the

isolation and 3D reconstruction of sulfur-related particles (Figure 2a). Comparing the charge (Figure 2b-i) and discharge (Figure 2b-ii) states of the first cycle, the sulfur distribution had already changed with a slight reduction in particle size after discharge, which is associated with an activation process particularly in high-loading sulfur electrodes. Notably, a decrease in sulfur loading and substantial redistribution were observed after 200 cycles (Figure 2b-iii), indicating considerable active material loss. This loss is most evident when comparing the sulfur density in the first charge state (Figure 2b-i) to that in the 200th open-circuit potential (OCP) state (Figure 2b-iii) and fully charged state (Figure 2b-iv), which demonstrates pronounced sulfur depletion after prolonged cycling. More pronounced morphological changes in sulfur particles are evident in the enlarged images presented in Supplementary Figure S5. Optical images of the pristine separator, as well as those retrieved from S/C and S/C/LGPS coin cells after 200 cycles, are shown in Supplementary Figure S20. Notably, only a slight yellowing is observed after cycling compared to the initial state, indicating very limited formation of soluble sulfur species during long-term operation. Given that sulfur conversion follows a QSS process, as previously discussed, we attribute this sulfur loss primarily to detachment from the electrode due to redistribution and volume changes rather than dissolution into the electrolyte. Crack formation within the electrode was identified (Figures 2c and S4b), which suggests the need for improved mechanical stability to maximise lifetime. To ensure proper functionality, the cell underwent one full charge–discharge cycle prior to X-CT analysis, as the assembly success rate for the 0.8 mm Swagelok cell is low, making prevalidation essential. Figure 2c presents the morphology of the standard S/C electrode after the initial cycle, revealing the presence of cracks. Following an additional discharge for lithiation, these cracks became slightly narrower due to the volumetric expansion of Li_2S relative to sulfur. However, after 200 cycles, significant crack enlargement was observed under both de-lithiated (4.0 V, Figure S4c) and OCP conditions. This deterioration is attributed to repeated expansion and contraction of the electrode during cycling, which is expected to be an important factor contributing to active material isolation or dislocation and by extension capacity loss. The morphological changes are more pronounced in the side-view X-CT images (Figure 2d). Focusing on a specific region (yellow rectangle in Figure 2d top left), the sulfur particles become noticeably smaller after a single discharge cycle (blue rectangle in Figure 2d top right). However, their 'charged-state' morphology remains largely unchanged after 200 cycles (yellow rectangle in Figure 2d bottom left), suggesting that sulfur particles tend to aggregate and recover their initial structure during charging, despite being dispersed into smaller particles during discharge. Notably, Li_2S particles exhibit continuous growth throughout cycling, which correlates with the observed capacity fade (blue solid rectangle in Figure 2d bottom right). A consistent trend is also observed and independently validated in Figure S4c. This

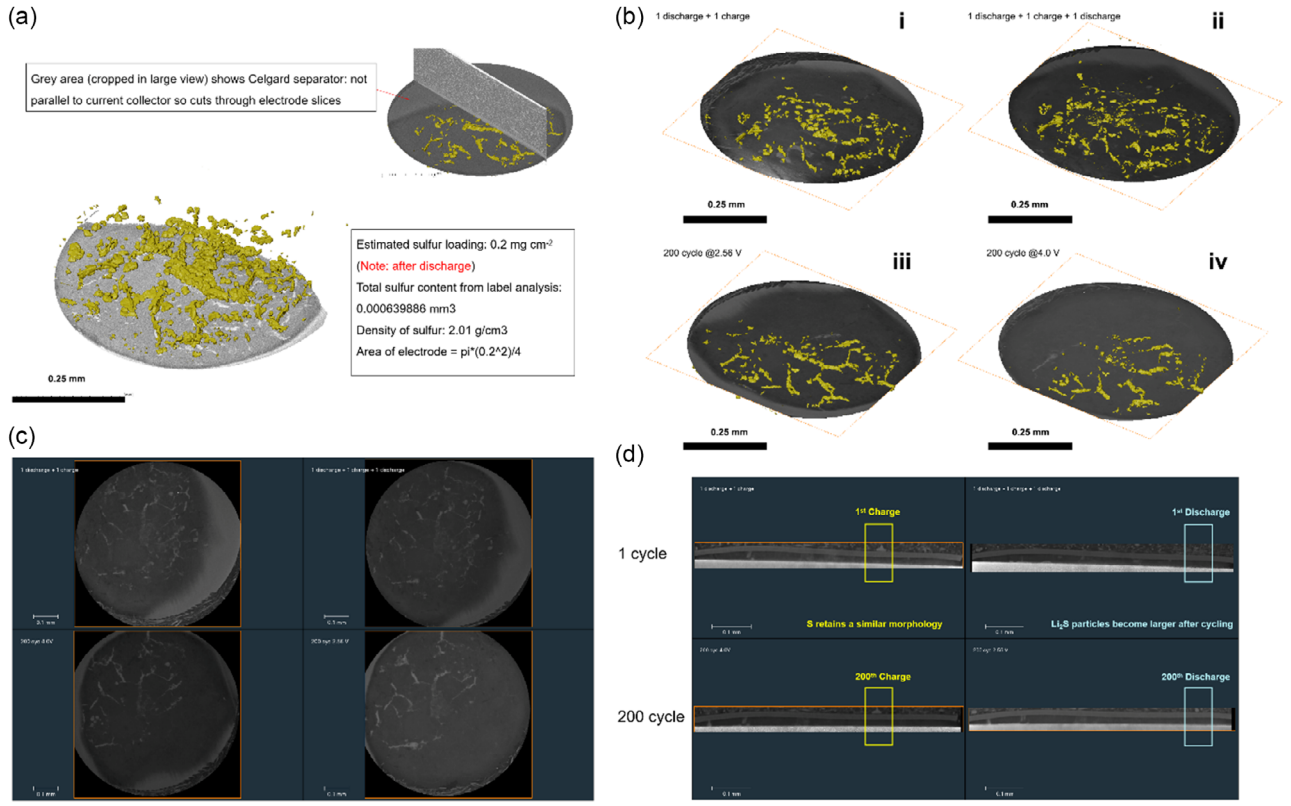

FIGURE 2 | (a) The separation of sulfur from standard S/C positive electrode in X-ray CT imaging; (b) the sulfur distribution of X-CT images for S/C positive electrode after: (a) 1 discharge and 1 charge @4.0 V; (b) 1 discharge and 1 charge followed by 1 discharge @ 1.0 V; (c) 200 cycles @4.0 V; (d) 200 cycles @2.56 V (OCP); (c) the top view and (d) side view of X-CT images for S/C positive electrode after: (top left) one discharge and one charge @4.0 V; (top right) one discharge and one charge followed by one discharge @ 1.0 V; (bottom left) 200 cycles @4.0 V; (bottom right) 200 cycles @2.56 V (OCP). All scalebars 0.1 mm.

indicates that sulfur redistribution occurs more prominently during discharge rather than charge, further underscoring the challenges of maintaining electrode integrity in QSS Li–S systems. This is in keeping with the formation of intermediate polysulfide species observed during discharge and discussed previously.

The morphology and elemental distribution of the Gelion S/C positive electrode were investigated by scanning electron microscopy (SEM) and energy-dispersive X-ray spectroscopy (EDS). As shown in Figure 3a, the electrode exhibits a heterogeneous microstructure composed of carbon flakes, carbon nanotubes, and sulfur agglomerates, forming an interconnected conductive network. The corresponding EDS elemental mapping (Figure 3b) reveals a homogeneous spatial distribution of carbon, sulfur, and the fluorine-containing binder across the electrode. The EDS spectrum (Figure 3c) confirms that C, S, and F are the dominant elements, while trace amounts of O (≈0.5 keV) and Si (≈1.7 keV) are also detected, which are likely associated with minor additives or background contamination. The individual elemental maps of C, S, and F (Figure 3d–f) further corroborate their uniform dispersion throughout the electrode matrix.

As shown in Figure 3g, the optical image of the S/C positive electrode exhibits a smooth surface even under high sulfur loading > 4 $mg_S\ cm^{-2}$, indicating that the presence of LGPS does not interfere with the coating process. The fabrication protocol for this S/C electrode was optimised using a PVDF-HFP binder and ethyl acetate as the solvent (optimisation details provided in Figure S2) due to the polar nature of n-methyl-2-pyrrolidone which reacts with LGPS. Coated electrodes with lower sulfur loading (2 $mg_S\ cm^{-2}$) also exhibit a similarly smooth surface (Figures S7, S8), indicating that the optimised protocol is a promising approach for incorporating polar-solvent-sensitive materials into electrodes and is comparable to the previously established standard protocol.

The sulfur distribution was inferred from contrast differences in X-CT based on known density and attenuation characteristics.

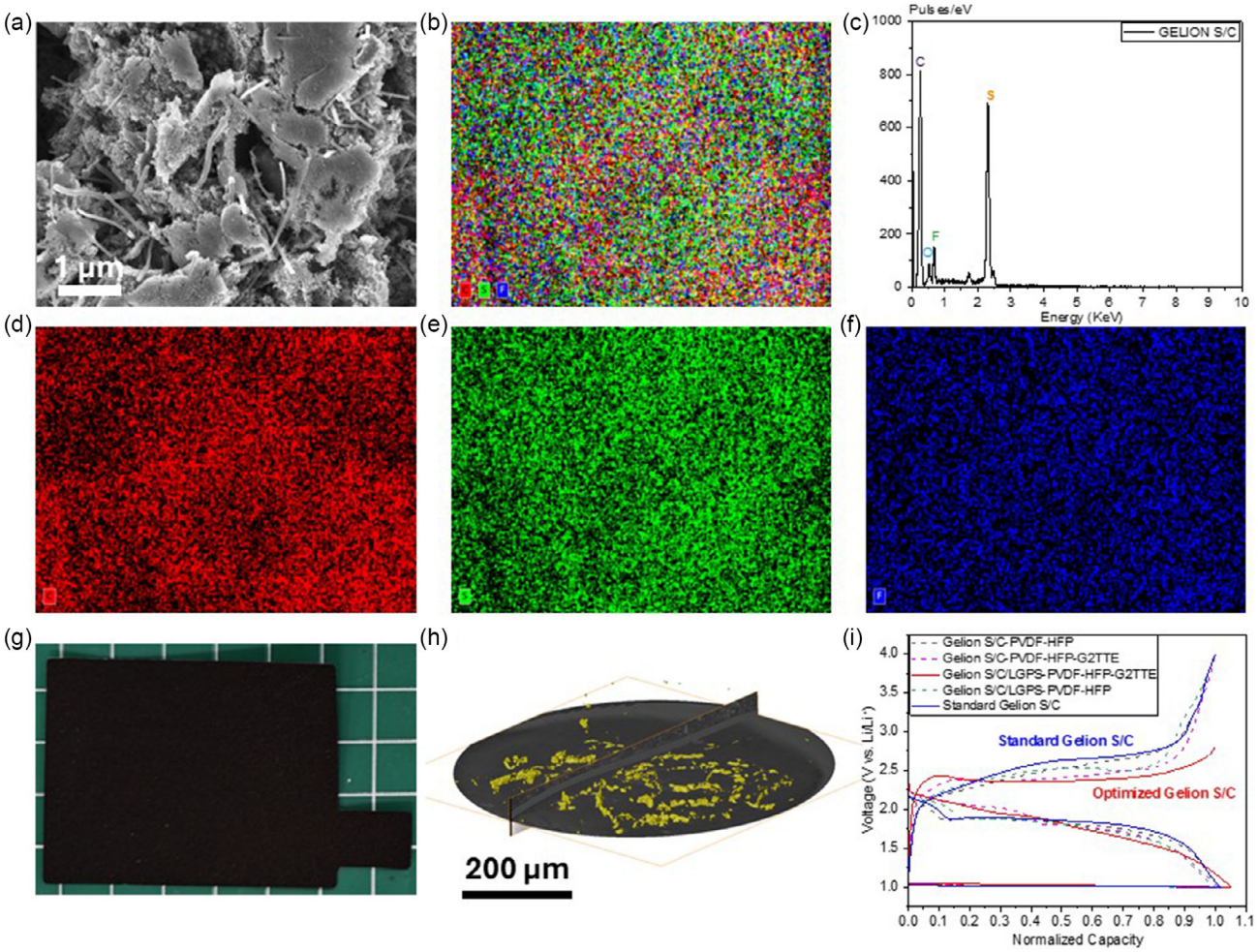

FIGURE 3 | (a) The typical SEM image of Gelion S/C positive electrode; (b) the sum elemental distribution of C, S, and F elements; (c) the EDS analysis of Gelion S/C positive electrode; the elemental distribution of (d) C, (e) S, and (f) F element; (g) the optical image (1 cm per line segment) of high loading Gelion S/C positive electrode coated on Al foil with a sulfur loading > 4 $mg_S\ cm^{-2}$; (h) the X-ray CT imaging of Gelion S/C positive electrode for sulfur distribution and morphology; and (i) the charge–discharge profiles for S/C positive electrodes w/wo addition of LGPS in various of binders and electrolytes [(the optimised one with addition of LGPS (red) displays a 200 mV decrease for overpotential compared to the standard one (blue)], where the overpotential is defined as the voltage difference between the charge and discharge plateaus at half of the normalized capacity.

The grey area (cropped in the large view) shows the Celgard separator, which is not parallel to the current collector and therefore cuts through the electrode slices. The particles highlighted in yellow were identified as active sulfur species within the electrode in its predischarge state (Figure 3h). To further enhance the reaction kinetics of QSS Li–S batteries, LGPS (10 wt%) was incorporated into the standard S/C positive electrode to improve Li-ion conductivity. The charge–discharge profiles, recorded within a voltage range of 1.0–4.0 V and normalized for direct comparison, are presented in Figure 3i. Notably, the addition of LGPS, along with binder and electrolyte optimisation, reduces the overpotential by ≈200 mV when compared to the standard electrode with similar loading to one with LGPS incorporated. The presence of LGPS improves local Li^+ transport and interfacial charge transfer, leading to earlier activation of the oxidation reaction (normalized capacity of 0.1) at a higher apparent voltage. This reduction is particularly evident during the charging process, while the discharge profile exhibits a single plateau, further supporting the QSS conversion of sulfur species. This improvement is attributed to the enhanced ionic conductivity and catalytic activity provided by LGPS, which facilitates the rapid transformation of sulfur intermediates.

The long-term cycling performance of cells incorporating LGPS in a G2–TTE electrolyte demonstrates reasonable stability, with capacity retention exceeding 60% after 100 cycles (Figure S17a). Although this is lower than that of cells without LGPS, the reported capacities are not optimised and should not be interpreted as the upper limit of the proposed electrode architecture. However, the rate performance of the LGPS + Gelion2 S/C electrode surpasses that of the electrode without LGPS, particularly at higher current rates such as 1C. At this rate, the LGPS-containing electrode delivers a capacity ≈200 mAh g^{-1} higher than that of the Gelion2 S/C electrode (Figure S17b). This result suggests that LGPS enhances ionic transport and represents a promising strategy for improving kinetics in solid-state batteries.

The cell with LGPS in Gen2 electrolyte shows lower stability compared to the G2-TTE electrolyte, likely due to the gradual degradation of LGPS in the Gen2 electrolyte (Figure S18). This degradation may also arise from the potential window in which the cell was cycled, which requires further optimisation for long-term stability and performance. The CV profiles provide further insight into the enhanced redox kinetics upon the incorporation of LGPS (Figure S19). During the cathodic scan (Figure S19a), both electrodes exhibit a similar first reduction peak at ~2.2 V, corresponding to the conversion of elemental sulfur to long-chain polysulfides (Li_2S_n, $n \geq 4$), indicating that LGPS has a limited effect on this initial step. In contrast, the second reduction peak at lower potentials, associated with the further conversion to short-chain species (Li_2S_2/Li_2S), shows a pronounced difference. The Gelion S/C + LGPS electrode displays a broader and higher-intensity peak, suggesting accelerated kinetics and enhanced utilization of active sulfur species in this stage. During the anodic scan (Figure S19b), the LGPS-containing electrode exhibits a lower onset potential and a higher oxidation peak current compared to the pristine Gelion S/C electrode, indicating reduced polarization and facilitated oxidation of Li_2S/Li_2S_2 back to higher-order polysulfides and sulfur. The shift toward lower overpotential and the increased peak intensity collectively demonstrate improved charge–transfer kinetics. Overall, these results confirm that the incorporation of LGPS effectively promotes both reduction and oxidation processes, particularly enhancing the kinetics of short-chain polysulfide conversion, thereby contributing to improved electrochemical performance.

Electrochemical impedance spectroscopy (EIS) was employed to further elucidate the effect of LGPS on interfacial charge–transfer behavior (Figure S20). In the fresh cells (Figure S20a), the LGPS + Gelion S/C electrode exhibits a noticeably smaller semicircle in the high-to-medium frequency region compared to the pristine Gelion S/C electrode, indicating a reduced charge–transfer resistance (R_{ct}). This suggests that the incorporation of LGPS facilitates faster electron/ion transport across the electrode–electrolyte interface. After cycling (Figure S20b), a similar trend is maintained, with the LGPS-containing electrode still showing a lower R_{ct} than the Gelion S/C counterpart. Although the impedance increases for both electrodes after prolonged cycling due to interfacial evolution, the LGPS-modified system demonstrates a more moderate increase, implying improved interfacial stability and sustained charge–transfer kinetics. Overall, the consistently lower R_{ct} values before and after cycling confirm that LGPS effectively enhances interfacial charge transport and contributes to improved electrochemical kinetics in the Li–S system. The coin cells were disassembled, and the separators from GELION S/C coin cells with and without LGPS were examined. Only limited polysulfide deposition was observed (Figure S21), indicating the QSS conversion of sulfide species.

The morphological evolution of the LGPS-containing S/C electrode was further examined using both SEM (Figure S22) and X-CT (Figure S23) to establish a direct correlation with electrochemical behavior. SEM images of the pristine electrodes show that the incorporation of LGPS does not significantly alter the initial morphology, as both electrodes exhibit comparable particle distribution and surface features. After cycling, however, the LGPS-containing electrode displays a more compact and fused structure, suggesting pronounced structural rearrangement and volume expansion. Consistent with these observations, X-CT analysis reveals that the pristine electrode possesses a relatively uniform sulfur distribution, whereas the cycled electrode shows clear densification accompanied by a substantial reduction in sulfur content, indicating severe sulfur loss. This combined evidence explains the electrochemical trends: although LGPS improves ionic transport and reduces polarization—leading to enhanced rate capability—it also accelerates structural evolution and active material depletion, resulting in inferior cycling stability. These findings establish a clear relationship between morphological changes and electrochemical performance in the LGPS-containing system.

3.3 | Pouch Cell Performance

Pouch cells were fabricated in a dry room, with the assembly process optimised from manual to automated stacking. The fabrication process began with the preparation of the S/C/LGPS positive electrode ink, which was uniformly coated onto Al foil under dry-room conditions (Figure 4a). The coated foil was then precisely cut into the designed electrode shape using a cutter (Figure 4b), and the active material mass was determined by measuring the weight difference between bare and coated electrodes. For the

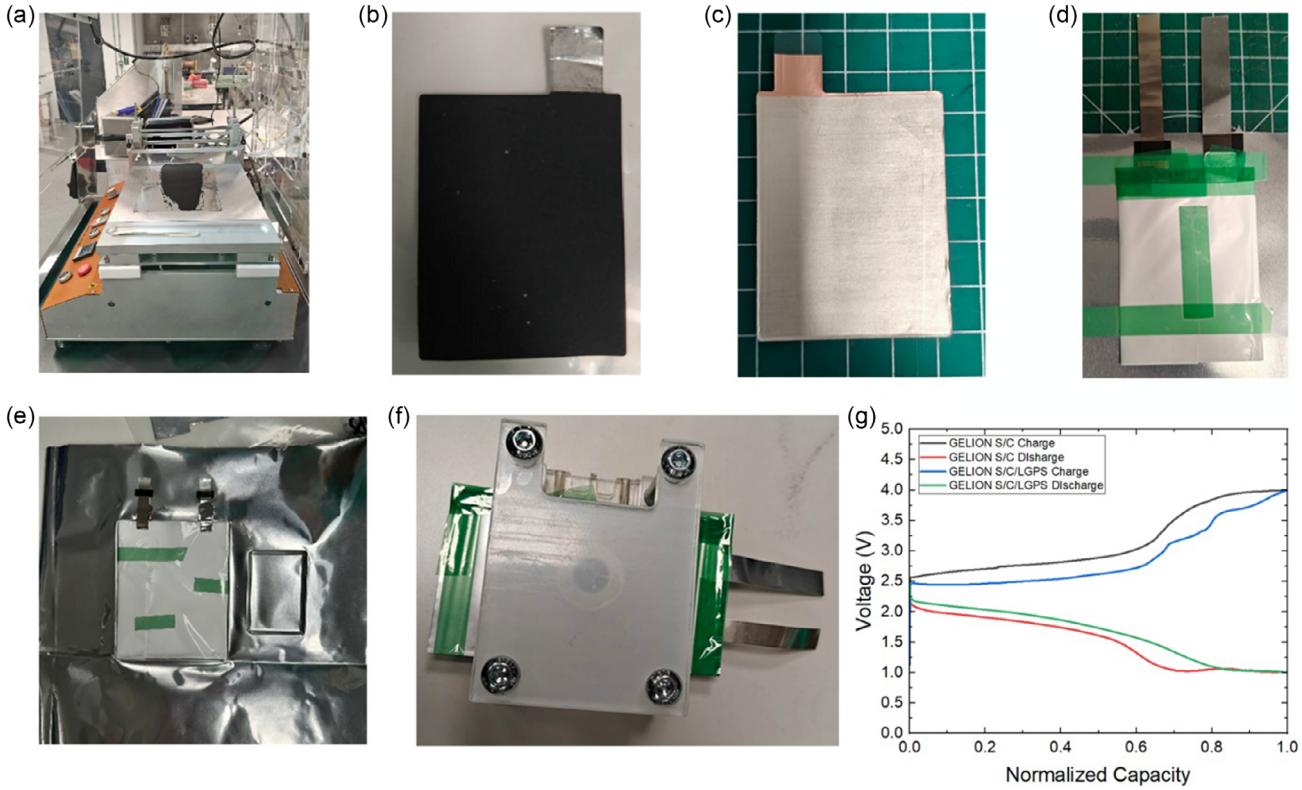

FIGURE 4 | (a) The S/C/LGPS electrode coating in the dry room for QSS Li–S battery; (b) the clipped S/C/LGPS electrode by a cutter with the tag area scraping off; (c) the clipped Li foil on Cu for Li–S pouch cells; (d) the battery core for Li–S pouch cell; (e) the battery core in the aluminium–plastic composite case; (f) the pouch cell after pressing; and (g) the charge–discharge profiles for S/C pouch cells w/wo addition of LGPS.

anode, lithium foil was laminated onto both sides of a copper foil current collector, leaving a designated area for tab welding (Figure 4c). Once the electrodes were prepared, the battery core was assembled by stacking the electrodes. Automated stacking significantly improved alignment, reducing the risk of short circuits and increasing fabrication efficiency (Figure 4d). The assembled battery core was then encased in an aluminium–plastic composite pouch (Figure 4e), with an additional smaller compartment designed to accommodate gas evolution during the first-cycle formation process. After vacuum sealing, excess pouch material was trimmed, resulting in a compact and final pouch cell was pressed in a module for testing (Figure 4f). Following process optimisation, pouch cells were fabricated with and without LGPS in the S/C positive electrode. The OCP of the S/C pouch cell without LGPS was measured at 2.396 V, while the addition of LGPS increased the OCP to 2.521 V (Figure S24). Electrochemical testing confirmed a reduction in overpotential by ≈200 mV in LGPS-containing cells, consistent with results observed in coin cells (Figure 4g). The cycling stability of the pouch cells was evaluated under galvanostatic conditions at C/100 to fully realize the available capacity. The S/C/LGPS pouch cells were functioning for 19 cycles with rational Charge/Discharge profiles (Figure S25) and then failed due to electrolyte leakage. Cells incorporating LGPS exhibited an improved performance (800 mAh/g with addition of LGPS vs. 600 mAh/g without addition of LGPS), characterised by higher capacity retention and lower polarization. These findings validate the scalability of the standard S/C system and highlight the potential of LGPS to enhance the performance of practical Li–S battery configurations in pouch cells [40–43].

4 | Conclusion

The study provides insights of the QSS mechanism in Li–S batteries, highlighting the critical role of sparingly soluble Li_2S_x ($x = 4.96$) and Li_2S_y ($y = 2.53$) intermediates in influencing electrochemical behavior and mitigating the shuttle effect. LGPS was found to be pivotal in enhancing reaction kinetics and improving sulfur utilisation. The reduced overpotential observed in LGPS-containing cells indicated significantly higher lithium-ion diffusion coefficients within the positive electrode. This improvement is attributed to the superior ionic conductivity and catalytic properties of LGPS, which facilitate the rapid conversion of QSS discharge products. It is also apparent that the cycle stability of the S/C/LGPS cell is slightly reduced due to the imperfect compatibility between the current binder and electrolyte, which necessitates further investigation. These findings offer valuable insights for optimising the design and composition of QSS Li–S batteries. This work advances the fundamental understanding of QSS Li–S battery mechanisms while demonstrating the potential of LGPS to accelerate kinetics and suppress polysulfide dissolution. Additionally, the successful fabrication and testing of pouch cells represent a crucial step toward scalability. Future research will focus on enhancing cycling stability and employing in situ diagnostic techniques to further refine these systems.

Acknowledgments

The authors acknowledge the Faraday Institution (Faraday.ac.uk; EP/S003053/1) for funding through the LiSTAR research programme

(FIRG083). J.R. and H.L. also thank Innovate UK for financial support (Project Number: 10 040 939). P.R.S. acknowledges the Royal Academy of Engineering Chair in Emerging Technologies (CiET1718 \59). Additionally, the authors would like to thank the technical staff at APL, in particular Joe Barwick, Rosalie Hamill, and Mark Buckwell for their support in pouch cell fabrication.

Funding

This study was supported by Faraday Institution (Grant FIRG083), Innovate UK (Grant 10040939), and Royal Academy of Engineering (Grant CiET1718\59).

Conflicts of Interest

Sharad Amin, Gareth Hartley and Adrien Amigues are employees of Gelion Ltd. a Li-S materials supplier and cell manufacturer.

Data Availability Statement

The data that support the findings of this study are available from the corresponding author upon reasonable request.

References

1. Y. Shao, B. Pang, L. Bird, J. B. Robinson, and P. R. Shearing, "Contemporary Trends in Lithium-Sulfur Battery Design: AComparative Review of Liquid, Quasi-Solid, and All-Solid-State Architectures and Mechanisms," *Advanced Energy Materials* 16 (2025): e03239, https://doi.org/10.1002/aenm.202503239.

2. W. Chen, T. Lei, C. Wu, et al., "Designing Safe Electrolyte Systems for a High-Stability Lithium–sulfur Battery," *Advanced Energy Materials* 8 (2018): 1702348.

3. H. Li, S. Ma, J. Li, et al., "Altering the Reaction Mechanism to Eliminate the Shuttle Effect in Lithium-Sulfur Batteries," *Energy Storage Materials* 26 (2020): 203–212.

4. X. Song, X. Liang, J. Eko, et al., "Toward Practical Li–S Batteries: On the Road to a New Electrolyte," *Advanced Energy Materials* 14 (2024): 2402506.

5. C. Zhao, K. Amine, and G.-L. Xu, "Nontraditional Approaches to Enable High-Energy and Long-Life Lithium–sulfur Batteries," *Accounts of Chemical Research* 56 (2023): 2700–2712.

6. G. Zhou, E. Paek, G. S. Hwang, and A. Manthiram, "Long-Life Li/Polysulphide Batteries with High Sulphur Loading Enabled by Lightweight Three-Dimensional Nitrogen/Sulphur-Codoped Graphene Sponge," *Nature Communications* 6 (2015): 7760.

7. A. Manthiram, S. H. Chung, and C. Zu, "Lithium–sulfur Batteries: Progress and Prospects," *Advanced Materials* 27 (2015): 1980–2006.

8. L. Zhu, N. Li, and P. R. N. Childs, "Light-Weighting in Aerospace Component and System Design," *Propulsion and Power Research* 7 (2018): 103–119.

9. H. T. Reid, G. Singh, E. Palin, et al., "Key Considerations for Cell Selection in Electric Vertical Take off and Landing Vehicles: A Perspective," *EES Batteries* 1 (2025): 227–241.

10. B. Qi, X. Hong, Y. Jiang, et al., "A Review on Engineering Design for Enhancing Interfacial Contact in Solid-State Lithium–sulfur Batteries," *Nano-Micro Letters* 16 (2024): 71.

11. K. Coke, M. J. Johnson, J. B. Robinson, A. J. E. Rettie, T. S. Miller, and P. R. Shearing, "Illuminating Polysulfide Distribution in Lithium Sulfur Batteries; Tracking Polysulfide Shuttle Using Operando Optical Fluorescence Microscopy," *ACS Applied Materials & Interfaces* 16 (2024): 20329–20340.

12. R. E. Owen, W. Du, J. Millichamp, P. R. Shearing, D. J. L. Brett, and J. B. Robinson, "Visualising the Effect of Areal Current Density on the Performance and Degradation of Lithium Sulfur Batteries Using Operando Optical Microscopy," *Journal of the Electrochemical Society* 171 (2024): 120523.

13. M. Safari, C. Y. Kwok, and L. F. Nazar, "Transport Properties of Polysulfide Species in Lithium–sulfur Battery Electrolytes: Coupling of Experiment and Theory," *ACS Central Science* 2 (2016): 560–568.

14. J. B. Robinson, K. Xi, R. V. Kumar, et al., "2021 Roadmap on Lithium Sulfur Batteries," *Journal of Physics: Energy* 3 (2021): 031501.

15. S. Badhrinathan, H. Dai, and G. P. Pandey, "Challenges and Approaches to Designing High-Energy Density Lithium-Sulfur Pouch Cells," *Batteries & Supercaps* 8 (2024): e202400544.

16. Y. Gong, J. Li, K. Yang, et al., "Towards Practical Application of Li–S Battery with High Sulfur Loading and Lean Electrolyte: Will Carbon-Based Hosts Win This Race?," *Nano-Micro Letters* 15 (2023): 150.

17. H. Li, Y. Gong, C. Fu, et al., "A Novel Method to Prepare a Nanotubes@ Mesoporous Carbon Composite Material Based on Waste Biomass and Its Electrochemical Performance," *Journal of Materials Chemistry A* 5 (2017): 3875–3887.

18. Y. Gong, C. Fu, A. Dong, H. Zhou, H. Li, and Y. Kuang, "Polar Ultrathin Self-Doping Carbon Nitride Nanosheets with Intrinsic Polysulfide Adsorption for High Performance Lithium-Sulfur Batteries," *Batteries & Supercaps* 1 (2018): 192–201.

19. H. Li, S. Ma, H. Cai, et al., "Ultra-Thin Fe_3C Nanosheets Promote the Adsorption and Conversion of Polysulfides in Lithium-Sulfur Batteries," *Energy Storage Materials* 18 (2019): 338–348.

20. Q. Miao, N. Solan, G. Hyun, J. Holoubek, and P. Liu, "Electrolyte Engineering for Long-Life Li-SPAN Batteries," *ACS Energy Letters* 8 (2023): 4818–4830.

21. A. L. Phan, P. M. L. Le, and C. Wang, "Realizing High-Energy and Long-Life Li/SPAN Batteries," *Joule* 8 (2024): 1601–1618.

22. A. L. Phan, B. Nan, P. M. L. Le, et al., "Lightweight Electrolyte Design for Li/Sulfurized Polyacrylonitrile (SPAN) Batteries," *Advanced Materials* 36 (2024): 2406594.

23. X. Zhao, C. Wang, Z. Li, X. Hu, A. Abdul Razzaq, and Z. Deng, "Sulfurized Polyacrylonitrile for High-Performance Lithium Sulfur Batteries: Advances and Prospects," *Journal of Materials Chemistry A* 9 (2021): 19282–19297.

24. J. Li, F. Xie, W. Pang, Q. Liang, X. Yang, and L. Zhang, "Regulate Transportation of Ions and Polysulfides in All–solid-State Li-S Batteries Using Ordered-MOF Composite Solid Electrolyte," *Science Advances* 10 (2024): eadl3925.

25. D. Wang, L.-J. Jhang, R. Kou, et al., "Realizing High-Capacity All-Solid-State Lithium-Sulfur Batteries Using a Low-Density Inorganic Solid-State Electrolyte," *Nature Communications* 14 (2023): 1895.

26. Q. Kang, Y. Li, Z. Zhuang, et al., "Dielectric Polymer Based Electrolytes for High-Performance All-Solid-State Lithium Metal Batteries," *Journal of Energy Chemistry* 69 (2022): 194–204.

27. L. Porcarelli, A. S. Shaplov, M. Salsamendi, et al., "Single-Ion Block Copoly(ionic Liquid)s as Electrolytes for All-Solid State Lithium Batteries," *ACS Applied Materials & Interfaces* 8 (2016): 10350–10359.

28. Z. Li, S. Zhang, S. Terada, et al., "Promising Cell Configuration for Next-Generation Energy Storage: Li2S/Graphite Battery Enabled by a Solvate Ionic Liquid Electrolyte," *ACS Applied Materials & Interfaces* 8 (2016): 16053–16062.

29. J. Li, F. Xie, W. Pang, Q. Liang, X. Yang, and L. Zhang, "Regulate Transportation of Ions and Polysulfides in All-Solid-State Li-S Batteries Using Ordered-MOF Composite Solid Electrolyte," *Science Advances* 10 (2024): eadl3925.

30. Y. Liu, Y. An, C. Fang, et al., "Surface-Localized Phase Mediation Accelerates Quasi-Solid-State Reaction Kinetics in Sulfur Batteries," *Nature Chemistry* 17 (2025): 1–10.

31. H. Song, K. Münch, X. Liu, et al., "All-Solid-State Li–S Batteries with Fast Solid–solid Sulfur Reaction," *Nature* 637 (2025): 1–8.

32. D. Wang, B. Gwalani, D. Wierzbicki, et al., "Overcoming the Conversion Reaction Limitation at Three-Phase Interfaces Using Mixed Conductors towards Energy-Dense Solid-State Li–S Batteries," *Nature Materials* 24 (2025): 1–9.

33. X. Gao, Z. Yu, J. Wang, et al., "Electrolytes with Moderate Lithium Polysulfide Solubility for High-Performance Long-Calendar-Life Lithium–sulfur Batteries," *Proceedings of the National Academy of Sciences* 120 (2023): e2301260120.

34. S. Kirchhoff, M. Fiedler, A. Dupuy, et al., "A Small Electrolyte Drop Enables a Disruptive Semisolid High-Energy Sulfur Battery Cell Design via an Argyrodite-Based Sulfur Cathode in Combination with a Metallic Lithium Anode," *Advanced Energy Materials* 14 (2024): 2402204.

35. B. Pang, H. Li, Y. Guo, et al., "A Quasi-Solid-State High-Rate Lithium Sulfur Positive Electrode Incorporating $Li_{10}GeP_2S_{12}$," *Communications Materials* 6 (2025): 175.

36. H. Yuan, H. J. Peng, J. Q. Huang, and Q. Zhang, "Sulfur Redox Reactions at Working Interfaces in Lithium–sulfur Batteries: A Perspective," *Advanced Materials Interfaces* 6 (2019): 1802046.

37. S. Lang, S.-H. Yu, X. Feng, M. R. Krumov, and H. D. Abruña, "Understanding the Lithium–sulfur Battery Redox Reactions via Operando Confocal Raman Microscopy," *Nature Communications* 13 (2022): 4811.

38. A. Yermukhambetova, C. Tan, S. Daemi, et al., "Exploring 3D Microstructural Evolution in Li-Sulfur Battery Electrodes Using in-Situ X-Ray Tomography," *Scientific Reports* 6 (2016): 35291, https://doi.org/10.1038/srep35291.

39. S. Zhou, J. Shi, S. Liu, et al., "Visualizing Interfacial Collective Reaction Behaviour of Li–S Batteries," *Nature* 621 (2023): 75–81.

40. X. Li, L. Yuan, D. Liu, J. Xiang, Z. Li, and Y. Huang, "Solid/Quasi-Solid Phase Conversion of Sulfur in Lithium–sulfur Battery," *Small* 18 (2022): 2106970.

41. H. Li, Y. Gong, H. Zhou, et al., "Ampere-Hour-Scale Soft-Package Potassium-Ion Hybrid Capacitors Enabling 6- Minute Fast-Charging," *Nature Communications* 14, no. 1 (2023): 6407.

42. H. Li, H. Chen, B. Pang, et al., "Van-der-Waals-Forces-Modulated Graphene-P-Phenyl-Graphene Carbon Allotropes," *Nature Communications* 16, no. 1 (2025): 10011.

43. S. Liu, H. Xu, Y. Ai, H. Li, Y. Bengio, and H. Guo, "Expert-Guided Llm Reasoning for Battery Discovery: From Ai-Driven Hypothesis to Synthesis and Characterization," arXiv preprint arXiv:2507.16110, (2025).

Supporting Information

Additional supporting information can be found online in the Supporting Information section.